Optimization of pH-universal O$_2$ reduction electrocatalysis by precise control over structural variables via basic bathing

Chuangchuang Yang, Peiyao Bai, Weiqi Liu, Shilin Wei, Wendu Zhang, Lang Xu [*]

MOE Key Laboratory of Coal Processing and Efficient Utilization, School of Chemical Engineering and Technology, China University of Mining and Technology, 1 Daxue Road, Xuzhou, Jiangsu 221116, China

ARTICLE INFO

ABSTRACT

In pursuit of finding alternatives to Pt for O$_2$ reduction reaction (ORR), biomass-based catalysts are promising candidates because of their low prices and comprehensive sources that just compensate for the drawbacks of Pt. However, it is difficult to determine unambiguously structure-function correlations of biomass-based catalysts due to their complex structures. Moreover, biomass-based metal-free ORR electrocatalysts often suffer from poor mass transport and pH applicability. Hence, tuning structural variables specifically, improving mass transport within porous domains, and achieving pH-universal catalytic activities are key to optimization of metal-free ORR electrocatalysts derived from biomass. In this study the 'basic bathing' method is proposed for precise control over structural variables of nitrogen-doped metal-free ORR electrocatalysts that originate from staple waste biomass—wheat straw. The basic bathing makes use of the fact that KOH can result in a series of physicochemical changes within lignocellulosic biomass and thereby re-proportion pore width distributions of synthesized materials. Under the action of basic bathing, the optimal electrocatalyst having the largest mesopore volume and the equal distribution of nitrogen species is superior in terms of pH-universal ORR electrocatalytic activity when compared to its non-basic-bathing counterparts. The structure-function analyses, benefiting from the specific tuning of mesopores by the basic bathing, demonstrate the linear relations between mesopore volumes and limiting current densities irrespective of pH. Furthermore, the density functional theory (DFT) calculations indicate the synergistic effects of pyridinic, pyrrolic and graphitic nitrogens at a 1:1:1 atomic ratio contribute to the decreased overpotential requirement. Taken together, the reproducible results provide compelling evidence for the importance of mesopores and nitrogen species distributions in enhancing the pH-universal ORR performance. In a broader context, the basic bathing is truly inspirational for niche exploitation of biomass for future energy technologies.

1. Introduction

Oxygen reduction reaction (ORR) is the cathodic half-reaction for plenty of electrochemical energy conversion devices exemplified by polymer electrolyte membrane fuel cells and metal-air fuel cells [1,2]. The relatively mature ORR electrocatalysts in the primary low-temperature fuel cell market comprise the noble metal Pt, which, because of its trace amount, high cost and poor tolerance for fuel-stream impurities, can limit its usefulness and large-scale applications [3,4]. Consequently, non-Pt materials are under intense investigation, expanding the armory of ORR electrocatalysts [5–7], among which metal-free carbon-based catalysts provide promising alternatives to Pt [8–10].

An accessible supply of cost-effective carbon sources is a prerequisite for large-scale production of carbon-based materials [11]. Different forms of lignocellulosic biomass, such as agricultural and forestry waste, are indeed inexpensive, abundant and renewable carbon sources [12]. Lignocellulosic biomass has long been used in the paper pulping and biofuel industries [13]. Aimed at achieving carbon neutrality worldwide, the non-fuel exploitation of biomass is of far-reaching importance for the sustainable development of resources and the environment [14]. As a niche application, exploring high-performance carbonaceous materials derived from biomass is potentially a very rich field [15–17].

There are several noticeable advantages of employing biomass to fabricate carbon-based materials: (a) biomass is an ideal carbon source alongside many merits including low cost, massive reserves and

---

numerous forms [18]; (b) part of biomass has intriguing structures that are otherwise hard to construct artificially [19]; (c) biochar is readily processed into functional solid-state materials by simple treatments such as heating and doping [20]. Such advantages that are the opposite of the deficiencies in Pt-based catalysts provide the basis for industrial preparations of high-performance biomass-based carbon materials as efficient electrocatalysts towards the ORR.

However, biomass-based carbon materials also have major drawbacks: (a) precise control over structural variables of biomass-based materials is particularly challenging, making it very difficult to establish how they work [21]; (b) due to the limitations of chemical activation methods, mass transport resistance is relatively high within porous domains of biomass-based materials [22]; (c) biomass-based metal-free carbon can have high catalytic activities towards the ORR in basic media but often demonstrate poor performance in both acidic and neutral electrolytes that are commonly found in fuel cell applications [23]. These problems need to be overcome.

Structures of biomass-based carbon materials depend strongly on processing temperatures, the variation of which can result in the simultaneous changes in a set of structural variables, such as surface area, pore volume and doping level [24]. The synchronous variation in various variables poses the major obstacle to unmasking structure-function relationships and understanding how to optimize catalytic performance. Therefore, we shall need to find ways to control precisely structural variables of biomass-based metal-free carbon materials like model catalysts—that is, varying a single variable while maintaining others, so that we can probe the influence of such variable on the performance and elucidate the structure-function correlations.

In this work we introduce the method of *basic bathing* to realize the precise control over structural variables of biomass-based metal-free ORR electrocatalysts. For the basic bathing processing, an alkali metal hydroxide (in this case, KOH) enables lignocellulosic framework structures of biomass to undergo swelling, dissolution and distortion, which can exert the specific influence over pore width distributions of biomass-based materials. We select a staple, widespread agricultural waste—wheat straw as the carbon source, which is readily converted into a group of nitrogen-doped metal-free porous carbon catalysts having similar physicochemical properties other than mesopores because of the basic bathing. The optimal material that contains the largest mesopore volume and the equal distribution of the three main nitrogen species displays the superior pH-universal ORR catalytic performance compared with its non-basic-bathing counterparts, commercial Pt/C as well as many recently reported catalysts. Further structure-function investigations demonstrate that the synergistic effects of graphitic, pyrrolic and pyridinic nitrogens help to decrease the overpotential required to drive the ORR and that the limiting current densities are directly proportional to the volumes of mesopores rather than micropores regardless of pH. Accordingly, our findings have important implications for workable solutions to the above-mentioned problems with biomass-based metal-free carbon catalysts.

2. Experimental section

2.1. Basic bathing

Straw from common wheat (*Triticum aestivum*) was collected, cleansed and dried before use. Then, wheat straw was pulverized into fine powder. The alkali metal hydroxide solution used for the basic bathing was prepared by dissolving 1 g of KOH in a 50 mL of ultrapure water (18 MΩ cm). During the course of basic bathing, a beaker containing the aqueous KOH solution was thermostatted at 70 °C, and 3 g of the powdered wheat straw were added to the basic solution and immersed for 2 h while stirring.

2.2. Catalyst preparation using the basic bathing

On completion of the basic bathing processing as described above, 3 g of $KHCO_3$ were transferred directly to the basic bathing mixture of KOH and wheat straw to consume KOH, followed by addition of melamine (3 g) to the mixture while stirring at 70 °C. The mixture was then placed in an 80 °C drying oven. Next, the dry mixture was heated under N_2 (flow rate: 80 cm^3 min^{-1}) in a temperature-programmable tube furnace (i.e., maintaining 300 °C for 2 h before further heating to 900 °C that was kept for additional 2 h; heating/cooling rates: 5 °C min^{-1}). After cooling to room temperature, the preliminary product underwent an acid wash for 2 h using 1 M HCl at 50 °C, followed by filtration and rinsing thoroughly with ultrapure water. The final product was obtained and denoted WSC-1 after drying (the initials WSC stand for wheat straw catalyst).

2.3. Catalyst preparation dispensing with the basic bathing

3 g of the powdered wheat straw were added to 50 mL of ultrapure water and the resulting suspension maintained at 70 °C was stirred for 2 h. Subsequently, 1 g of KOH, 3 g of $KHCO_3$ and 3 g of melamine were delivered sequentially to the wheat straw suspension (KOH → $KHCO_3$ → melamine) while stirring at 70 °C. The suspension was then transferred to an oven and allowed to dry. The rest of the procedure is the same as described in Section 2.2. The product obtained by this procedure was denoted WSC-2.

In addition, an aqueous suspension of the powdered wheat straw (3 g) in 50 mL of ultrapure water was stirred at 70 °C for 2 h. Next, 3 g of $KHCO_3$ and 3 g of melamine were added in sequence to the suspension ($KHCO_3$ → melamine) while stirring at 70 °C. The suspension was subsequently left to dry in an oven. The remaining procedure is the same as described in Section 2.2. The product prepared using this procedure was denoted WSC-3.

2.4. Structural characterization, electrochemical measurements and theoretical calculations

The details of physicochemical characterization and electrocatalytic O_2-reduction experiments on catalysts were outlined in the Supplementary material. All the density functional theory (DFT) calculations were made using the Gaussian 16 software [25,26]. The detailed information on the DFT calculations was also given in the Supplementary material.

3. Results and discussion

3.1. Roles of basic bathing

Like the bulk of lignocellulosic biomass, wheat straw contains the three categories of organic compounds, that is, cellulose, hemicellulose and lignin, which are highly cross-linked with each other and provide structural supports for plants [27]. Cellulose is polymerized by thousands of glucose molecules via the glycosidic linkages, with extensive hydrogen bonding formed by the hydroxyl groups of D-glucose units, thus endowing cellulose with the high mechanical strength [27]. Cellulose cannot dissolve in water, but an alkali metal hydroxide is able to take part in a complex series of interactions with cellulose by breaking hydrogen bonds, resulting in the swelling of hydrogen bonding networks [28,29]. Compared to cellulose, hemicellulose and lignin can be partially dissolved in aqueous solutions of alkali metal hydroxides, thereby forming cavities within the internal structure of biomass and leading to weakening of the cross-linking strength of the three components [27]. Overall, from a microscopic perspective (Fig. 1a), the basic bathing can lead to the swelling, dissolution and distortion of lignocellulosic frameworks, hence loosening compact textures and expanding pore widths of internal biomass, which is favorable for the accessibility
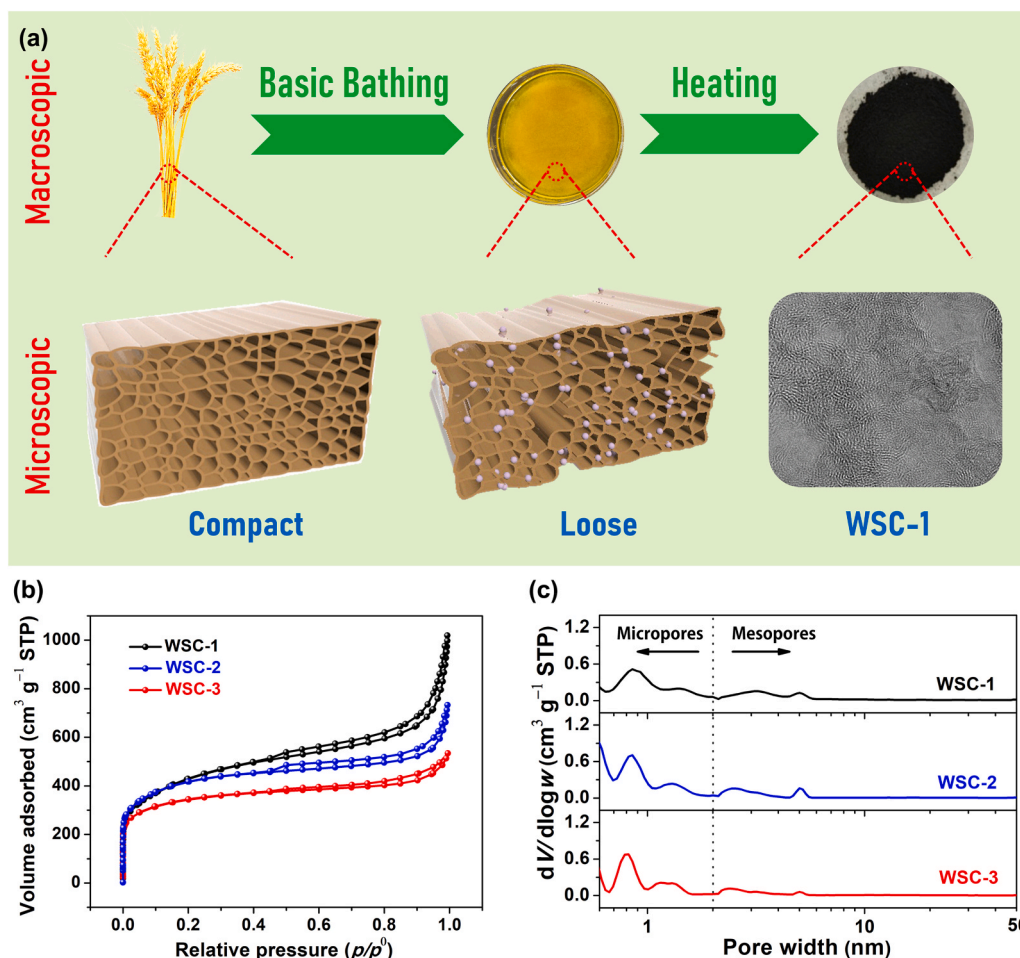
Fig. 1. Schematic representation illustrating how the basic bathing transforms wheat straw into WSC-1 from the macroscopic and microscopic perspectives (a). N_2 adsorption-desorption isotherms (b) and pore width distributions (c) of WSC-1, WSC-2 and WSC-3.

of external chemical reagents and the specific modulations of pore width distributions.

Wheat straw undergoes the heating treatment following the basic bathing processing. To eliminate the direct discharge of KOH into the environment and enhance its utilization, this alkali metal hydroxide is not filtered out after the basic bathing. However, KOH can react with the nitrogen dopant melamine in which the amino groups are replaced, which weakens the doping effect. Hence, an excess of $KHCO_3$ has been used to avoid this weakening because bicarbonate can convert caustic KOH into mild K_2CO_3, and the resulting K_2CO_3 as well as the remaining $KHCO_3$ jointly act as the potassium-based pore formers. After that, we add melamine to the wheat straw/K_2CO_3/$KHCO_3$ assembly followed by heating under pure nitrogen, eventually obtaining the product WSC-1 (Fig. 1a).

To elucidate the effects of basic bathing, the control sample WSC-2 has been prepared using the same amounts of KOH, $KHCO_3$ and melamine as WSC-1 except that this control sample dispenses with the treatment of basic bathing. Fig. 1b exhibits the nitrogen adsorption-desorption isotherms of WSC-1 and WSC-2. For both samples, the uptakes of nitrogen are high when the relative pressure p/p^0 is lower than 0.01, indicating the presence of large quantities of micropores (assigned to the Type I isotherm) [30]; meanwhile, the marked hysteresis loops at $p/p^0 > 0.45$ originate from mesopores (belonging to the Type H4 loop) [30]. Adopting the quenched solid density functional theory, the pore width distributions of WSC-1 and WSC-2 are shown in Fig. 1c, where the two samples indeed include the coverages of both micropores and mesopores. Further, there is a slight difference in the mesopore regions:

WSC-1 has the two peaks centered at 3.2 nm and 5.0 nm whereas the peak positions of WSC-2 turn out to be at 2.5 nm and 5.0 nm. Table S1 illustrates the surface and pore properties of WSC-1 and WSC-2. It can be identified that the two samples have very similar surface areas (WSC-1: 1430.18 $m^2 g^{-1}$, WSC-2: 1409.16 $m^2 g^{-1}$) but quite distinct pore volumes (WSC-1: 1.230 $cm^3 g^{-1}$, WSC-2: 0.903 $cm^3 g^{-1}$), which are ascribed to the discrepancy in mesopores. The mesopore of WSC-1 has the considerably larger volume than that of WSC-2, while their micropore volumes are similar, implying the basic bathing increases the pore volume of WSC-1 through the enlargement of mesopores, which can also be reflected by its pore width distribution as the 2.5-nm peak shifts to 3.2 nm. This is because the basic bathing results in the deformation of inner structures of wheat straw as mentioned earlier.

In addition, the second control sample WSC-3 has been made for understanding the respective roles of basic bathing and pore formers. By comparing the preparative conditions of the two control samples, neither WSC-2 nor WSC-3 goes through the basic bathing. Without the addition of KOH, WSC-3 gains the smaller amount of pore formers (that is, 3 g $KHCO_3$) than WSC-2 (that is, 1 g KOH and 3 g $KHCO_3$). The pore width distributions of WSC-2 and WSC-3 show noticeable similarity to each other (Fig. 1c), and the volumes of micropores and mesopores of WSC-2 are larger than their WSC-3 counterparts (Table S1), indicating that the potassium-based pore formers lead to the non-specific increase in pore volumes of both micropores and mesopores and that the more the pore formers, the larger are their resulting pore volumes. From Table S1, it should be noted that the surface areas of WSC-1, WSC-2 and WSC-3 are quite similar to each other ($S_{WSC-2}/S_{WSC-1} = 0.99$ and $S_{WSC-3}/$

$S_{\text{WSC-1}} = 0.92$) whereas the difference in their pore volumes is greatly magnified ($V_{\text{WSC-2}}/V_{\text{WSC-1}} = 0.73$ and $V_{\text{WSC-3}}/V_{\text{WSC-1}} = 0.58$). Furthermore, when comparing the volumes of micropores and mesopores of WSC-1, WSC-2 and WSC-3, it can be found that the basic bathing has considerable impact on mesopore volume ($^{meso}V_{\text{WSC-2}}/^{meso}V_{\text{WSC-1}} = 0.57$ and $^{meso}V_{\text{WSC-3}}/^{meso}V_{\text{WSC-1}} = 0.40$), yet little effect on micropore volume ($^{micro}V_{\text{WSC-2}}/^{micro}V_{\text{WSC-1}} = 1.11$ and $^{micro}V_{\text{WSC-3}}/^{micro}V_{\text{WSC-1}} = 0.99$). Consequently, the basic bathing can re-proportion pore width distributions, raise mesopore volumes specifically (in contrast to the potassium-based pore formers) and optimize mass transport within porous domains
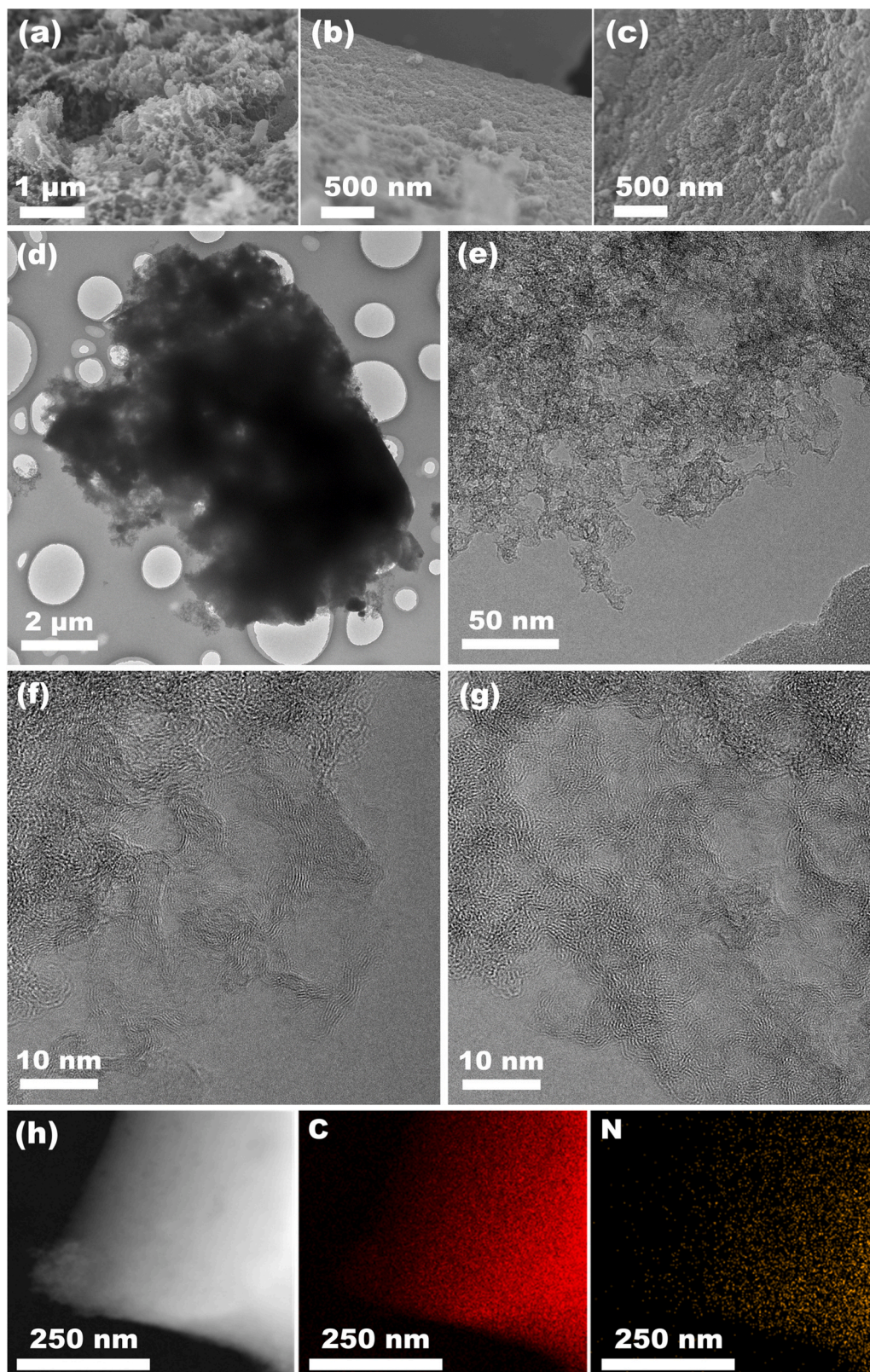

Fig. 2. SEM images of WSC-1 (a), WSC-2 (b) and WSC-3 (c). TEM (d–g) and elemental mapping (h) images of WSC-1.

while maintaining a high level of surface areas.

Electron microscopy methods provide the direct visualization of pore structures and surface textures of materials. It can be evidently seen from the scanning electron microscope (SEM) images that WSC-1 has the more surface roughness than the two control samples (Fig. 2a–c). The greater degree of surface roughness is capable of exposing more active sites to oxygen (along with electrolyte) and therefore promoting the ORR kinetics [31]. The markedly increased surface roughness of WSC-1 corroborates the evidence that a large number of smaller molecules dissolved and disaggregated during the basic bathing undergo the re-aggregation at the high-temperature heating stage and result in the rough surface, which can also be observed in the transmission electron microscope (TEM) images. As seen from Fig. 2d, e, the edges of WSC-1 take on the disordered, porous and gauze-like character able to provide large surface area and pore volume (consistent with its physisorption data). Since the basic bathing causes a series of changes in the structures and compositions of lignocellulosic biomass, large amounts of inorganic and organic matter are leached from the original zones, leading to the loosening of intrinsic textures and the weakening of compactness (Fig. 2d). The gauze-like carbon films with well-developed pores are generated when dissolved molecules tend to agglomerate on the surface and edges at high temperatures (Fig. 2e). The high-resolution TEM images (Fig. 2f, g) present the marked lattice fringes that distort around the pores, exhibiting both a high degree of disorder in the porous carbon framework structures and some level of graphitization character. The elemental mapping analyses by the energy-dispersive X-ray spectroscopy (Fig. 2h) exhibit the uniform distribution of nitrogen atoms doped across the material surface, demonstrating that the basic bathing allows the close contact between the lignocellulosic biomass and the chemical reagents and therefore results in the well-dispersed nitrogen-doped porous carbon.

The wide-scan X-ray photoelectron spectroscopy (XPS) spectra of WSC-1, WSC-2 and WSC-3 (Fig. S1) each present the C 1s, N 1s and O 1s signals. The nitrogen amounts of WSC-1, WSC-2 and WSC-3 are 2.39 at %, 2.75 at% and 2.49 at%, respectively, which are very close to each other owing to the same heating temperatures. As displayed in Fig. 3a, each nitrogen signal can be split into four peaks that are ascribed to oxidized N, graphitic N, pyrrolic N and pyridinic N, among which the latter three are considered to be inextricably linked with the ORR activity [32]. The atomic ratios of graphitic N to pyrrolic N to pyridinic N in the WSC-series samples are quite similar (Fig. 3b), namely, 1:0.99:0.92 for WSC-1, 1:1.02:1.03 for WSC-2 and 1:0.95:0.97 for WSC-3. These data indicate that the basic bathing has little impact on the doping levels and distributions of nitrogen. Moreover, the X-ray diffraction (XRD) patterns of WSC-1, WSC-2 as well as WSC-3 are presented in Fig. 3c. The two weak bands centered at 24° and 43° in each pattern can be assigned to (002) and (100), respectively [32]. The broad bands show the overwhelmingly amorphous forms of the materials, which are consistent with the high-resolution TEM observations as described above. It is worth noting that the XRD patterns of the three materials made at the same heating temperature show great similarity to each other, implying the irrelevance of the basic bathing to the amorphous structures. Likewise, there is a close resemblance among the Raman spectra of WSC-1, WSC-2 and WSC-3 (Fig. 3d). The I_D/I_G values obtained from the Raman spectra can reflect the disorder characters of carbonaceous materials [33]. The I_D/I_G values of WSC-1, WSC-2 and WSC-3 are 0.98, 0.97 and 0.95, respectively. The similar I_D/I_G values indicate the basic bathing processing has little effect on the disorder degrees of the WSC-series samples.

In short, the physicochemical properties of WSC-1 and its non-basic-bathing counterparts bear close resemblances to each other apart from their mesopore volumes caused by the basic bathing. This characteristic is conducive to investigating and understanding the relationships between structures and electrocatalytic performance at various pH values
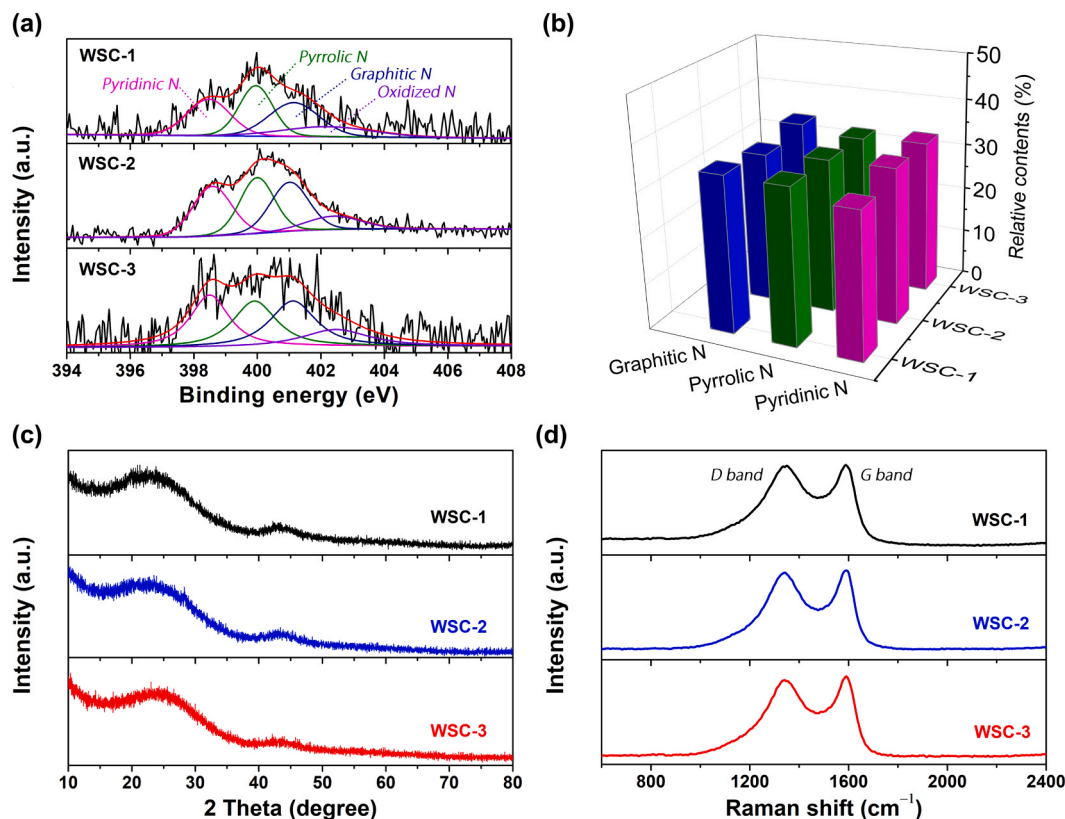

Fig. 3. Deconvolutions of nitrogen 1s XPS spectra (a), a three-dimensional representation of the relative contents of graphitic, pyrrolic and pyridinic nitrogens (b), XRD patterns (c) and Raman spectra (d) of WSC-1, WSC-2 and WSC-3.

that range from acidity to alkalinity.

3.2. Reactivity, selectivity and stability at different pH

In general terms, the ORR catalytic activities of metal-free carbon materials are markedly lower in acidic and neutral pH electrolytes than in basic ones. To probe pH applicability, the comparisons of electrocatalytic activities of WSC-1, WSC-2 and WSC-3 relative to a reference catalyst Pt/C in the acidic, basic and neutral electrolytes have been drawn using the linear sweep voltammetry method. All the potentials for the ORR electrocatalysis at different pH are scaled to the reversible hydrogen electrode (RHE). Fig. 4a–c illustrate the results in 0.5 M H_2SO_4, 0.1 M KOH and 0.1 M potassium phosphate buffer solution (PBS, pH = 7.0): WSC-1 has the higher limiting current densities (acidic: 6.18 mA cm^{-2}, basic: 6.52 mA cm^{-2} and neutral: 6.03 mA cm^{-2}) than the other two samples and Pt/C (Table 1), regardless of pH, and it is worthwhile to note that there is a positive correlation between the limiting current densities of the three samples and their corresponding mesopore volumes. This trend can be rationalized by considering that limiting current densities rely heavily on mass transport within reaction zones and are therefore closely related to their mesopore properties. Among the three biomass-based samples, the highest limiting current density of WSC-1 can be attributed to its largest mesopore volume created by the basic bathing, because their other major physicochemical properties (e.g. surface area, micropore volume, amorphousness and disorder degree) are close to each other. Additionally, the Tafel slopes can reflect the electrochemical kinetics [34]. The Tafel slopes of WSC-1 in the acidic, basic and neutral electrolytes are all smaller than those of Pt/C (Fig. 4d–f), indicating the improved electrocatalytic kinetics of the former. Hence, WSC-1 possesses the optimal catalytic capability for the pH-universal ORR, compared with its non-basic-bathing counterparts and many recently reported electrocatalysts (Table 1).

Selectivities of WSC-1 and Pt/C have been investigated using the rotating ring-disc electrode method. For fuel cells, an energetically advantageous ORR is expected to be the four-electron process and, in addition, the product of the four-electron ORR is water or hydroxide depending on pH, which is more favorable to activity and stability of an electrocatalyst than the competitive two-electron product peroxide [45]. As shown in Fig. 5a–c, the peroxide yields of WSC-1 in the acidic, basic and neutral solutions are 1.63%, 1.93% and 1.83%, respectively, all of which are smaller than their Pt/C counterparts in the corresponding electrolytes (acidic: 2.54%, basic: 4.01% and neutral: 4.29%). The electron-transfer numbers of WSC-1 under the acidic, basic and neutral conditions are 3.97, 3.96 and 3.96, respectively, larger than those of Pt/C (acidic: 3.95, basic: 3.92 and neutral: 3.92), demonstrating WSC-1 offers the four-electron ORR. Consequently, the optimal material has the higher selectivity than Pt/C in terms of the pH-universal ORR.

Stabilities of WSC-1 relative to Pt/C in the acidic, basic and neutral electrolytes have also been researched. Fig. 5d–f display the chronoamperometric data of WSC-1 and Pt/C in the H_2SO_4, KOH and PBS solutions. The currents under the catalysis of WSC-1 are quite stable and capable of keeping 93.7%, 96.3% and 95.5% of the initial values after 40,000 s (~ 11.1 h) in the acidic, basic and neutral electrolytes, respectively; by contrast, the declining rates of currents by Pt/C in the three different solutions are remarkably faster (merely maintaining 63.6% in H_2SO_4, 68.8% in KOH and 70.6% in PBS), exhibiting the high stability of WSC-1 over a wide range of pH. To further demonstrate the pH-universal robustness of WSC-1, the accelerated stress test (AST) protocol can also be used with the assistance of the square wave technique (Fig. S2). After the prolonged 30,000 cycles, WSC-1 still shows the similar polarization curves to its initial states, regardless of pH (Fig. 5g–i). Quantitatively, WSC-1 retains 93.8%, 92.0% and 90.4% of the initial current densities (at 0.2 V vs. RHE) after 30,000 cycles in the acidic, basic and neutral electrolytes, respectively, which are fully consistent with the chronoamperometric data mentioned above. Indeed, WSC-1 possesses the truly excellent pH-universal durability.

3.3. Relationships between reactivity and structure: from the standpoints of thermodynamics and mass transport

As summarized in Table 1, the onset potentials of WSC-1, WSC-2 and WSC-3 are virtually the same, irrespective of pH, although there is clear
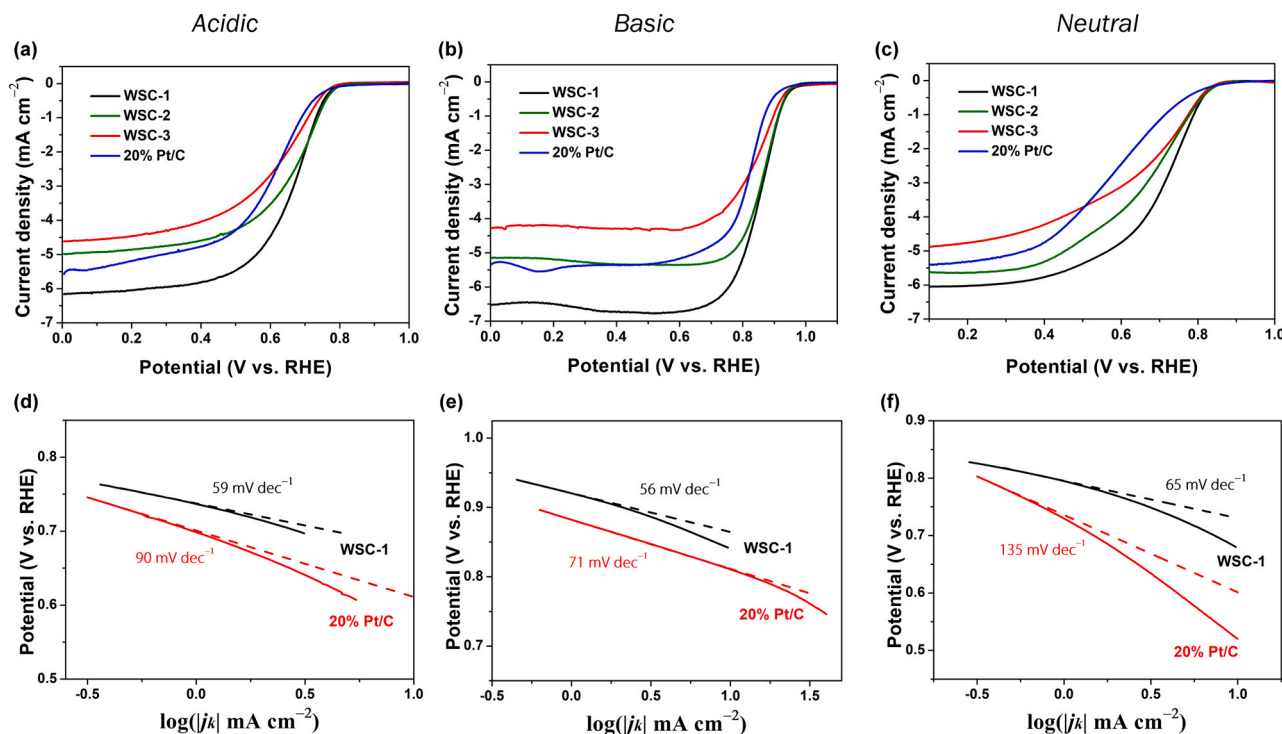

Fig. 4. Linear sweep voltammograms of WSC-1, WSC-2 and WSC-3 by comparison with Pt/C (a–c) and Tafel plots of WSC-1 and Pt/C indicated by the corresponding Tafel slopes (d–e) in the acidic (0.5 M H_2SO_4), basic (0.1 M KOH) and neutral (0.1 M PBS) solutions.

Table 1

Comparisons of the electrocatalytic activities towards the pH-universal ORR for basic-bathing WSC-1, its non-basic-bathing counterparts and recently reported catalysts.[a]

Material	0.5 M H_2SO_4			0.1 M KOH			0.1 M PBS		
	E_{onset}	$E_{1/2}$	J_L	E_{onset}	$E_{1/2}$	J_L	E_{onset}	$E_{1/2}$	J_L
WSC-1	**0.82**	**0.66**	**6.18**	**1.00**	**0.86**	**6.52**	**0.89**	**0.71**	**6.03**
WSC-2	0.82	0.67	5.00	1.00	0.87	5.14	0.89	0.68	5.62
WSC-3	0.82	0.63	4.61	0.99	0.85	4.31	0.88	0.67	4.90
20% Pt/C	0.82	0.60	5.55	0.98	0.82	5.37	0.88	0.58	5.41
CPNC-5-850 [35]	0.80	0.64	4.60	0.97	0.84	4.96	0.87	0.65	4.90
PS-900 [36]	0.82	0.70	5.10	1.00	0.85	5.84	0.90	0.73	5.52
ANDC-900–10 [37]	0.84	0.66	4.97	1.01	0.87	5.50	0.91	0.74	5.45
β-FeOOH/PNGNs [38]	0.84	0.68	4.55	1.02	0.88	5.10	0.86	0.69	5.10
NPF-CNS-2 [39]	0.83	0.70	5.03	0.90	0.81	5.42	0.70	0.58	4.23
Fe-N-C-NH₃ [40]	0.92	0.65	4.50	0.98	0.85	5.10	0.86	0.65	5.00
Co/NCA [41]	0.77[b]	0.65[b]	7.10[b]	0.95	0.83	6.00	0.84	0.70	5.00
Co–C-16 [42]	0.80	0.67	4.30	0.92	0.86	5.40	0.72[c]	0.63[c]	4.50[c]
PNFc-900 [43]	0.82	0.60	3.30	1.01	0.86	5.53	0.91	0.61	3.60
Fe@BC-800 [44]	0.86	0.70	4.70	1.01	0.85	5.30	0.86	0.68	4.20

[a] E_{onset}: onset potential (V vs. RHE); $E_{1/2}$: half-wave potential (V vs. RHE); J_L: limiting current density (mA cm^{-2}).
[b] Acidic electrolyte used is 0.1 M $HClO_4$ (pH = 1).
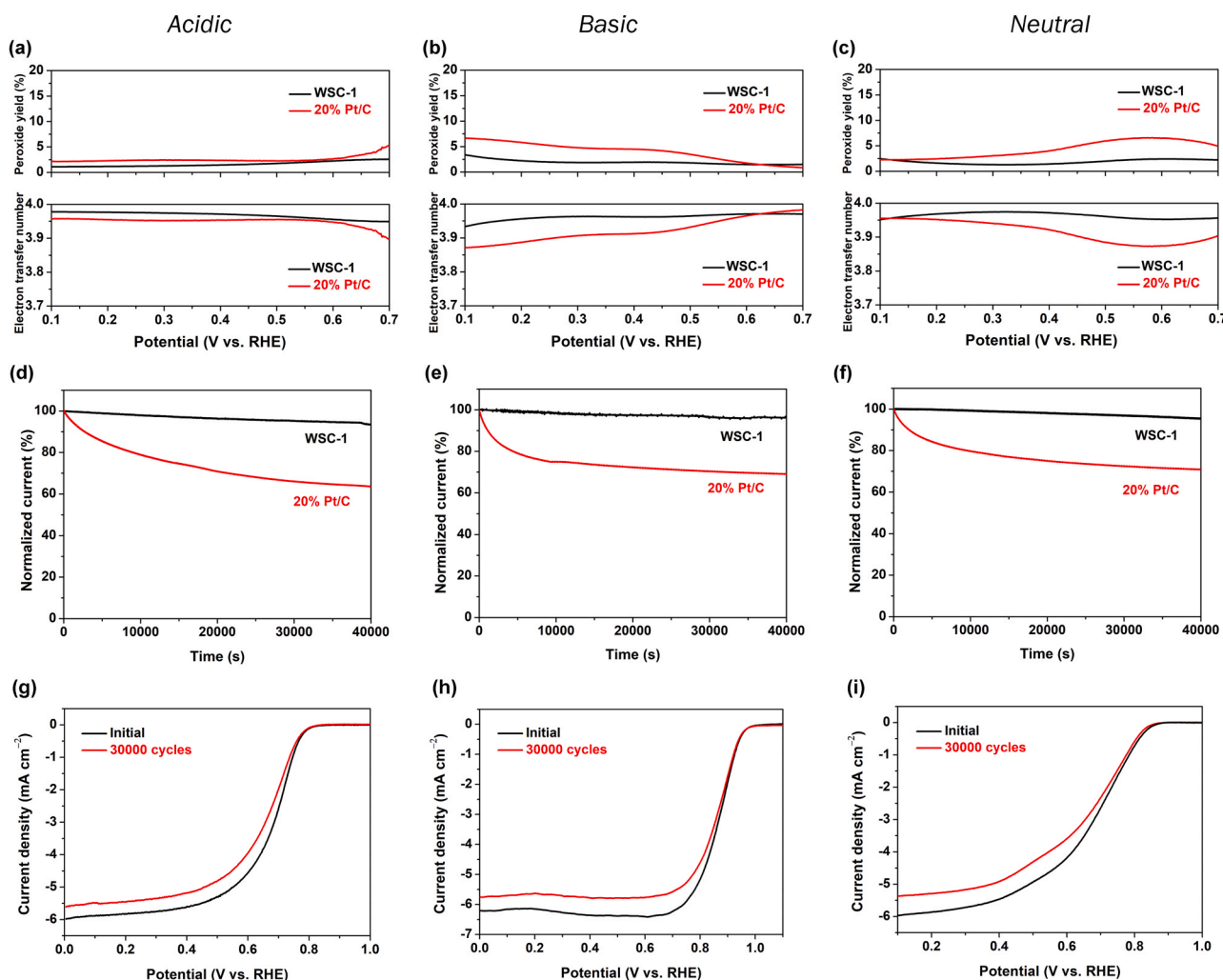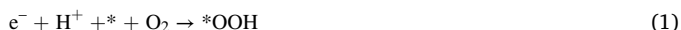[c] Neutral electrolyte used is 0.05 M PBS.

Fig. 5. Peroxide yields along with electron transfer numbers (a–c) and dependences of currents on time (d–f) of WSC-1 and Pt/C, together with linear sweep voltammograms of WSC-1 before and after 30,000 cycles (g–i), in the acidic, basic and neutral solutions.

distinction between their limiting current densities, which are of great relevance to their structures. Let us discuss the dependence of onset potentials first. As described above, the atomic percentages of nitrogen doped into WSC-1, WSC-2 and WSC-3 bear resemblance to each other and the atomic ratios of graphitic N to pyrrolic N to pyridinic N in the three samples are close to 1:1:1. To assess the impacts of nitrogen species

distributions on the reaction thermodynamics and onset potentials, a set of graphene clusters with different combinations of the nitrogen species has been constructed, as displayed in Fig. S3. The nomenclature for these clusters doped with nitrogen is quite straightforward in that graphitic N, pyrrolic N and pyridinic N are denoted grN, prN and pdN, respectively, with the overall 1:1 ratio between them.

Furthermore, the four-electron ORR process can be written as the following steps [46,47]:

$$e^- + H^+ + * + O_2 \rightarrow {}^*OOH \tag{1}$$

$$e^- + H^+ + {}^*OOH \rightarrow H_2O + {}^*O \tag{2}$$

$$e^- + H^+ + {}^*O \rightarrow {}^*OH \tag{3}$$

$$e^- + H^+ + {}^*OH \rightarrow H_2O + {}^* \tag{4}$$

where the asterisk * refers to an adsorption site. Such steps have also been illustrated in Fig. 6a. Following the computational method (see the Supplementary material), the Gibbs free energies of each step mentioned above for all the constructed clusters have been calculated at the ideal
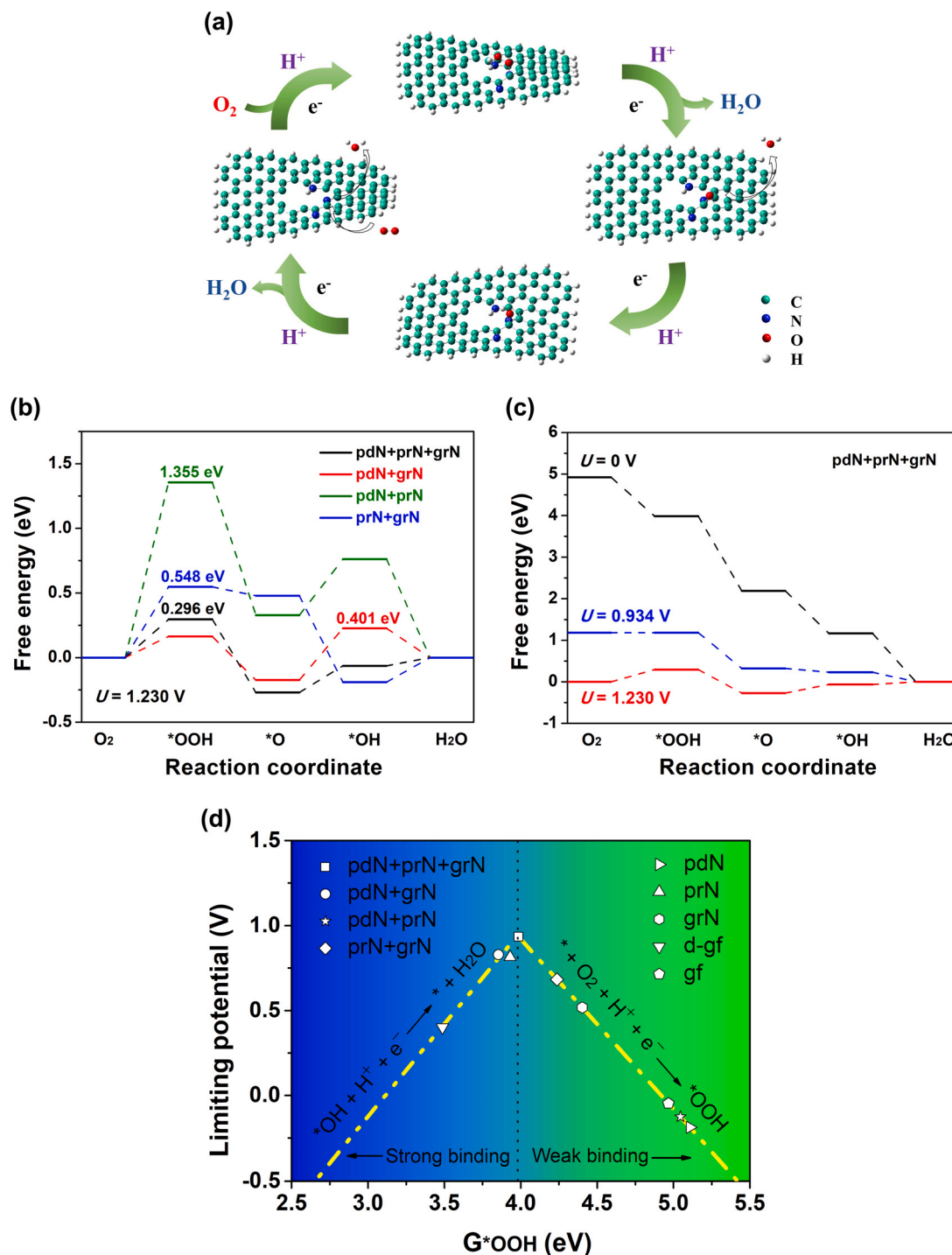

Fig. 6. Schematic diagram of the reaction steps involved in the 4-electron ORR (a). DFT-calculated free energy profiles of the representative clusters at 1.230 V (b) and of the pdN+prN+grN cluster at various potentials (c). The volcano plot depicting the dependences of limiting potentials on G_{*OOH} for all the constructed clusters (d).

thermodynamic potential of 1.230 V for the ORR, as summarized in
Table S2, while those for the four representative clusters are charted in
Fig. 6b. The highest free energy barriers of the clusters pdN+prN+grN,
pdN+grN, prN+grN and pdN+prN, related to the potential-determining
step ('thermodynamic bottleneck') for the ORR [48], are 0.296 eV,
0.401 eV, 0.548 eV and 1.355 eV, respectively. It follows that the
potential-determining step for pdN+prN+grN, prN+grN or pdN+prN is
the first step described above (the formation of *OOH) whereas the third
step (the generation of *OH) is potential determining for pdN+grN.
Obviously, the lower the Gibbs free energy barrier concerning the
potential-determining step, the more energetically favorable is the ORR
[48]. The pdN+prN+grN cluster, reflecting the pdN:prN:grN ratios of
1:1:1 for the WSC-series samples, can minimize the free energy barrier
for the potential-determining step and the overpotential losses for the
ORR. The optimized adsorption structures of the oxygenated in-
termediates on the pdN+prN+grN cluster are given in Fig. S4. The bond
lengths of key intermediates can be calculated and evaluated using
quantum mechanics, and in this case, the oxygen–oxygen bond length of
*OOH [47]. As shown in Table S3, this bond property for pdN+prN+grN
possesses the largest value, which indicates the marked weakening and
readily separation of the O–O bond into O atoms by this cluster.

Fig. 6c exhibits the Gibbs free energies of the reaction steps for the
pdN+prN+grN cluster at different applied potentials. At 1.230 V (the
thermodynamic equilibrium electrode potential for the ORR at standard
temperature and pressure), the Gibbs free-energy change (ΔG) at the
potential-determining step is greater than zero, which means that the
ORR at this equilibrium potential cannot occur spontaneously until extra
electrical work must be done. When the potential is shifted in a negative
direction to 0.934 V, ΔG at the potential-determining step decreases to
zero, indicating that the reaction will spontaneously proceed beyond
this limiting potential. Thus, at 0 V, the Gibbs free energies of the re-
action steps present the energetically *downhill* paths, displaying the
feature of spontaneous reactions. For all the clusters concerning the
ORR, the overpotentials that are the differences between equilibrium
potentials and limiting potentials have been listed in Table S2. Clearly,
the pdN+prN+grN cluster has the minimal overpotential requirement
among all the clusters because of the synergistic effects of pyridinic,
pyrrolic and graphitic nitrogens [32].

Fig. 6d displays the distribution of limiting potentials for the nine
clusters versus their respective G_{*OOH} (a descriptor that reflects the
binding strength between the key intermediate *OOH and a certain
cluster), known as the *volcano plot* [48,49]. It is obvious that
pdN+prN+grN at the apex of the volcano plot presents the largest
limiting potential among all the clusters, indicating the one with the
moderate binding strength has the minimal overpotential for the ORR.
By comparison, the binding strengths for the other clusters lying on the
either side of the volcano plot are either too strong or too weak, thereby

leading to the larger overpotential requirements, in accord with the
Sabatier principle [48]. Accordingly, WSC-1, WSC-2 and WSC-3, all with
the pdN:prN:grN ratios of approximately 1:1:1, have the commonly
small overpotentials.

Next, we discuss the dependence of limiting current density. WSC-1,
WSC-2 and WSC-3 have a set of structural variables in common with the
exception of mesopores. As mentioned earlier, all the limiting current
densities across a wide range of pH values are positively correlated with
the mesopore volumes of the three materials. It is further found that the
limiting current densities of WSC-1, WSC-2 and WSC-3 in either acidic or
basic or neutral electrolytes are directly proportional to their corre-
sponding mesopore volumes (Fig. 7a). This is not surprising given that
limiting current densities depend on mass transport that is closely
related to mesopore properties within porous domains. The greater the
mesopore volume, the more efficient is the mass transport, leading to the
higher limiting current density. For comparison, the dependences of
limiting current densities on micropore volumes of WSC-1, WSC-2 and
WSC-3 have been exhibited in Fig. 7b. Clearly, the limiting current
densities are not proportional to the micropore volumes. In other words,
for the acidic, basic and neutral ORR, there exist the linear relations
between limiting current densities and volumes of mesopores rather
than micropores. This general trend demonstrates that mesopores pro-
vide plenty of available active sites and efficient mass transport, whereas
micropores that enable the reaction interface roughness to increase
markedly fail to outperform mesopores in terms of mass transport
enhancement. Consequently, the reproducible data demonstrate that
increasing mesopore volumes through the basic bathing processing can
increase limiting current densities in the acidic, basic and neutral
electrolytes.

Interestingly, the order of slopes for the fitted lines at various pH
values (Fig. 7a) is basic > acidic > neutral, which means that the effects
of mesopores on mass transport are not the same in different electro-
lytes. More exactly, tuning mesopore volumes has the most dramatic
effect on the mass transport and the attendant limiting current density
when employing KOH as the electrolyte, the next for H_2SO_4 and the least
for PBS, which most likely arise from physicochemical inhomogeneity
among the different electrolyte ions, including hydrated radius, ion
mobility and molar conductivity [50].

4. Conclusions

To summarize, this research demonstrates how the basic bathing can
tune mesopores specifically while leaving other structural variables
unchanged. Following the basic bathing processing, the optimal elec-
trocatalyst WSC-1 has the higher catalytic activity towards the pH-
universal ORR than its non-basic-bathing counterparts in the acidic,
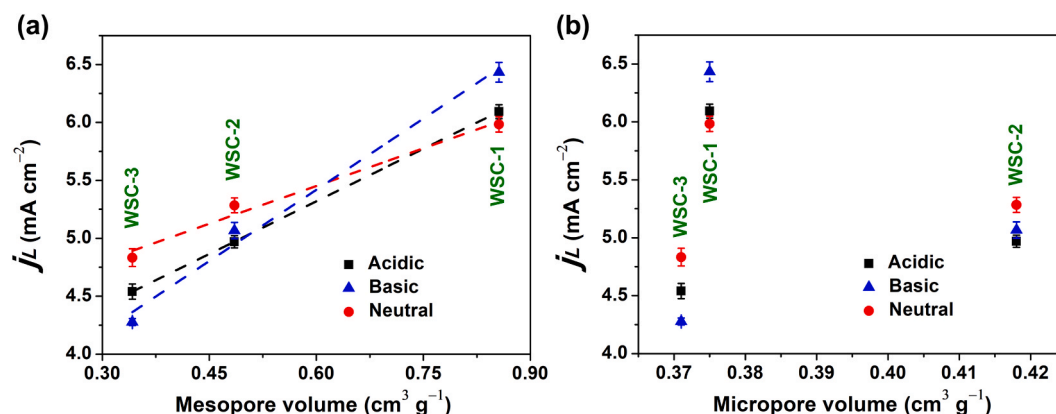basic and neutral electrolytes, which can be attributed to its largest

Fig. 7. Dependences of limiting current densities on mesopore volumes (a) and micropore volumes (b) of WSC-1, WSC-2 and WSC-3 in the acidic, basic and neutral solutions.

mesopore volume and the equal distribution of nitrogen species. Importantly, our reproducible results, which combine detailed experimental measurements and theoretical calculations, reveal the linear relations between mesopore volumes and limiting current densities regardless of pH as well as the synergistic effects of pyridinic, pyrrolic and graphitic nitrogens on overpotential requirements. Such structure-function relationships provide useful and rational routes to great enhancement in electrocatalytic activities of biomass-based metal-free carbon materials. Were we to regard this research only from a chemist's perspective, biomass could be processed into technologically and economically useful materials using the simple approach affording precise control of important structural variables, the same as found in purely chemical sources. Viewed from the sustainable standpoint, on the other hand, this research is giving interesting insights into the niche utilization of biomass for new energy technologies. It is therefore timely to exploit the rich repertoire of available biomass by this basic bathing method for exciting interdisciplinary researches at the forefront of catalytic science.

CRediT authorship contribution statement

Chuangchuang Yang: Investigation, Software, Validation, Data curation, Formal analysis, Visualization, Writing – original draft, Writing – review & editing. **Peiyao Bai:** Investigation, Software, Validation, Formal analysis. **Weiqi Liu:** Investigation, Validation, Formal analysis. **Shilin Wei:** Validation, Formal analysis. **Wendu Zhang:** Investigation, Formal analysis. **Lang Xu:** Conceptualization, Methodology, Resources, Writing – original draft, Writing – review & editing, Supervision, Project administration, Funding acquisition.

Declaration of Competing Interest

The authors declare that they have no known competing financial interests or personal relationships that could have appeared to influence the work reported in this paper.

Acknowledgments

Appendix A. Supplementary material

Supplementary data associated with this article can be found in the online version at doi:10.1016/j.apcatb.2021.120912.

References

[1] S. Yi, X. Qin, C. Liang, J. Li, R. Rajagopalan, Z. Zhang, J. Song, Y. Tang, F. Cheng, H. Wang, M. Shao, Insights into KMnO$_4$ etched N-rich carbon nanotubes as advanced electrocatalysts for Zn-air batteries, Appl. Catal. B Environ. 264 (2020), 118537.

[2] H.A. Firouzjaie, W.E. Mustain, Catalytic advantages, challenges, and priorities in alkaline membrane fuel cells, ACS Catal. 10 (2020) 225–234.

[3] Z. Ma, Z.P. Cano, A. Yu, Z. Chen, G. Jiang, X. Fu, L. Yang, T. Wu, Z. Bai, J. Lu, Enhancing oxygen reduction activity of Pt-based electrocatalysts: from theoretical mechanisms to practical methods, Angew. Chem. Int. Ed. 59 (2020) 18334–18348.

[4] S. Zaman, L. Huang, A.I. Douka, H. Yang, B. You, B.Y. Xia, Oxygen reduction electrocatalysts toward practical fuel cells: progress and perspectives, Angew. Chem. Int. Ed. 60 (2021) 17832–17852.

[5] T.J. Omasta, X. Peng, H.A. Miller, F. Vizza, L. Wang, J.R. Varcoe, D.R. Dekel, W. E. Mustain, Beyond 1.0Wcm^{-2} performance without platinum: the beginning of a new era in anion exchange membrane fuel cells, J. Electrochem. Soc. 165 (2018) J3039–J3044.

[6] X. Peng, T.J. Omasta, E. Magliocca, L. Wang, J.R. Varcoe, W.E. Mustain, Nitrogen-doped carbon-CoO$_x$ nanohybrids: a precious metal free cathode that exceeds 1.0Wcm^{-2} peak power and 100h life in anion-exchange membrane fuel cells, Angew. Int. Ed. 58 (2019) 1046–1051.

[7] H. Adabi, A. Shakouri, N. Ul Hassan, J.R. Varcoe, B. Zulevi, A. Serov, J. R. Regalbuto, W.E. Mustain, High-performing commercial Fe-N-C cathode electrocatalyst for anion-exchange membrane fuel cells, Nat. Energy 6 (2021) 834–843, https://doi.org/10.1038/s41560-021-00878-7.

[8] L. Yang, J. Shui, L. Du, Y. Liu, L. Dai, Z. Hu, Carbon-based metal-free ORR electrocatalysts for fuel cells: past, present and future, Adv. Mater. 31 (2019), 1804799.

[9] Q. Lv, N. Wang, W. Si, Z. Hou, X. Li, X. Wang, F. Zhao, Z. Yang, Y. Zhang, C. Huang, Pyridinic nitrogen exclusively doped carbon materials as efficient oxygen reduction electrocatalysts for Zn-air batteries, Appl. Catal. B Environ. 261 (2020), 118234.

[10] J. Lilloja, E. Kibena-Põldsepp, A. Sarapuu, A. Kikas, V. Kisand, M. Käärik, M. Merisalu, A. Treshchalov, J. Leis, V. Sammelselg, Q. Wei, S. Holdcroft, K. Tammeveski, Nitrogen-doped carbide-derived carbon/carbon nanotube composites as cathode catalysts for anion exchange membrane fuel cell application, Appl. Catal. B Environ. 272 (2020), 119012.

[11] L. Fagiolari, F. Bella, Carbon-based materials for stable, cheaper and large-scale processable perovskite solar cells, Energy Environ. Sci. 12 (2019) 3437–3472.

[12] B.M. Matsagar, R.X. Yang, S. Dutta, Y.S. Ok, K.C.W. Wu, Recent progress in the development of biomass-derived nitrogen-doped porous carbon, J. Mater. Chem. A 9 (2021) 3703–3728.

[13] E. Mäki, H. Saastamoinen, K. Melin, D. Matschegg, H. Pihkola, Drivers and barriers in retrofitting pulp and paper industry with bioenergy for more efficient production of liquid, solid and gaseous biofuels: a review, Biomass Bioenergy 148 (2021), 106036.

[14] Y. Wang, M. Zhang, X. Shen, H. Wang, H. Wang, K. Xia, Z. Yin, Y. Zhang, Biomass-derived carbon materials: controllable preparation and versatile applications, Small 17 (2021) 2008079.

[15] M. Borghei, J. Lehtonen, L. Liu, O.J. Rojas, Advanced biomass-derived electrocatalysts for the oxygen reduction reaction, Adv. Mater. 30 (2018) 1703691.

[16] P. Brachi, Synthesis of carbon dots (CDs) through the fluidized bed thermal treatment of residual biomass assisted by γ-alumina, Appl. Catal. B Environ. 263 (2020), 118361.

[17] J.L. Santos, C. Megías-Sayago, S. Ivanova, M.Á. Centeno, J.A. Odriozola, Functionalized biochars as supports for Pd/C catalysts for efficient hydrogen production from formic acid, Appl. Catal. B Environ. 282 (2021), 119615.

[18] X. Tang, D. Liu, Y.J. Wang, L. Cui, A. Ignaszak, Y. Yu, J. Zhang, Research advances in biomass-derived nanostructured carbons and their composite materials for electrochemical energy technologies, Prog. Mater. Sci. 118 (2021), 100770.

[19] J. Sun, Z. Wu, C. Ma, M. Xu, S. Luo, W. Li, S. Liu, Biomass-derived tubular carbon materials: progress in synthesis and applications, J. Mater. Chem. A 9 (2021) 13822–13850.

[20] S. Ye, G. Zeng, X. Tan, H. Wu, J. Liang, B. Song, N. Tang, P. Zhang, Y. Yang, Q. Chen, X. Li, Nitrogen-doped biochar fiber with graphitization from *Boehmeria nivea* for promoted peroxymonosulfate activation and non-radical degradation pathways with enhancing electron transfer, Appl. Catal. B Environ. 269 (2020), 118850.

[21] S. Tabac, D. Eisenberg, Pyrolyze this paper: can biomass become a source for precise carbon electrodes? Curr. Opin. Electrochem. 25 (2021), 100638.

[22] W. Zhang, C. Yang, W. Liu, H. Wang, S. Wei, J. Qi, P. Bai, B. Jin, L. Xu, Long-range order, short-range disorder: Engineering one-dimensional flow channel arrays with hierarchically porous reaction interfaces for electrocatalytic reduction of oxygen, Appl. Catal. B Environ. 293 (2021), 120199.

[23] W. Zhang, J. Qi, P. Bai, H. Wang, L. Xu, High-level nitrogen-doped, micro/mesoporous carbon as an efficient metal-free electrocatalyst for the oxygen reduction reaction: optimizing the reaction surface area by a solvent-free mechanochemical method, New J. Chem. 43 (2019) 10878–10886.

[24] J. Qi, W. Zhang, W. Zhou, L. Xu, Dual potassium salt-assisted lyophilization of natural fibres for the high-yield synthesis of one-dimensional carbon microtubes for supercapacitors and the oxygen reduction reaction, New J. Chem. 44 (2020) 6297–6311.

[25] M.J. Frisch, G.W. Trucks, H.B. Schlegel, G.E. Scuseria, M.A. Robb, J.R. Cheeseman, G. Scalmani, V. Barone, G.A. Petersson, H. Nakatsuji, X. Li, M. Caricato, A.V. Marenich, J. Bloino, B.G. Janesko, R. Gomperts, B. Mennucci, H.P. Hratchian, J.V. Ortiz, A.F. Izmaylov, J.L. Sonnenberg, Williams, F. Ding, F. Lipparini, F. Egidi, J. Goings, B. Peng, A. Petrone, T. Henderson, D. Ranasinghe, V.G. Zakrzewski, J. Gao, N. Rega, G. Zheng, W. Liang, M. Hada, M. Ehara, K. Toyota, R. Fukuda, J. Hasegawa, M. Ishida, T. Nakajima, Y. Honda, O. Kitao, H. Nakai, T. Vreven, K. Throssell, J.A. Montgomery Jr., J.E. Peralta, F. Ogliaro, M.J. Bearpark, J.J. Heyd, E.N. Brothers, K.N. Kudin, V.N. Staroverov, T.A. Keith, R. Kobayashi, J. Normand, K. Raghavachari, A.P. Rendell, J.C. Burant, S.S. Iyengar, J. Tomasi, M. Cossi, J.M. Millam, M. Klene, C. Adamo, R. Cammi, J.W. Ochterski, R.L. Martin, K. Morokuma, O. Farkas, J.B. Foresman, D.J. Fox, Gaussian 16, Revision B.01, Wallingford, CT, 2016.

[26] R. Dennington, T.A. Keith, J.M. Millam, GaussView, Version 6, Semichem Inc., Shawnee Mission, KS, 2016.

[27] R.C. Sun, Cereal Straw as a Resource for Sustainable Biomaterials and Biofuels—Chemistry, Extractives, Lignins, Hemicelluloses and Cellulose, Elsevier, Oxford, 2010.

[28] D. Klemm, B. Philipp, T. Heinze, Y. Heinze, W. Wagenknecht, Comprehensive Cellulose Chemistry, Wiley-VCH, Weinheim, 1998.

[29] H. Qi, Q. Yang, L. Zhang, T. Liebert, T. Heinze, The dissolution of cellulose in NaOH-based aqueous system by two-step process, Cellulose 18 (2011) 237–245.

[30] M. Thommes, K. Kaneko, A.V. Neimark, J.P. Olivier, F. Rodriguez-Reinoso, J. Rouquerol, K.S.W. Sing, Physisorption of gases, with special reference to the

evaluation of surface area and pore size distribution (IUPAC Technical Report), Pure Appl. Chem. 87 (2015) 1051–1069.

[31] J. Qi, W. Zhang, L. Xu, Solvent-free mechanochemical preparation of hierarchically porous carbon for supercapacitor and oxygen reduction reaction, Chem. Eur. J. 24 (2018) 18097–18105.

[32] P. Bai, W. Liu, C. Yang, S. Wei, L. Xu, Boosting electrochemical performance of activated carbon by tuning effective pores and synergistic effects of active species, J. Colloid Interface Sci. 587 (2021) 290–301.

[33] W. Liu, J. Qi, P. Bai, W. Zhang, L. Xu, Utilizing spatial confinement effect of N atoms in micropores of coal-based metal-free material for efficiently electrochemical reduction of carbon dioxide, Appl. Catal. B Environ. 272 (2020), 118974.

[34] Y. Wang, N. Xu, R. He, L. Peng, D. Cai, J. Qiao, Large-scale defect-engineering tailored tri-doped graphene as a metal-free bifunctional catalyst for superior electrocatalytic oxygen reaction in rechargeable Zn-air battery, Appl. Catal. B Environ. 285 (2021) 119811.

[35] J. Qi, B. Jin, W. Liu, W. Zhang, L. Xu, Converting coals into carbon-based pH-universal oxygen reduction catalysts for fuel cells, Fuel 285 (2021), 119163.

[36] L. Yu, C. Yang, W. Zhang, W. Liu, H. Wang, J. Qi, L. Xu, Solvent-free synthesis of N-doped nanoporous carbon materials as durable high-performance pH-universal ORR catalysts, J. Colloid Interface Sci. 575 (2020) 406–415.

[37] H. Wang, W. Zhang, P. Bai, L. Xu, Ultrasound-assisted transformation from waste biomass to efficient carbon-based metal-free pH-universal oxygen reduction reaction electrocatalysts, Ultrason. Sonochem. 65 (2020), 105048.

[38] Y. Li, J. Huang, X. Hu, L. Bi, P. Cai, J. Jia, G. Chai, S. Wei, L. Dai, Z. Wen, Fe vacancies induced surface FeO_6 in nanoarchitectures of N-doped graphene protected β-FeOOH: effective active sites for pH-universal electrocatalytic oxygen reduction, Adv. Funct. Mater. 28 (2018) 1803330.

[39] Y. Zheng, H. Song, S. Chen, X. Yu, J. Zhu, J. Xu, K.A.I. Zhang, C. Zhang, T. Liu, Metal-free multi-heteroatom-doped carbon bifunctional electrocatalysts derived from a covalent triazine polymer, Small 16 (2020) 2004342.

[40] Z. Chen, D. Zhao, C. Chen, Y. Xu, C. Sun, K. Zhao, M.A. Khan, D. Ye, H. Zhao, J. Fang, X.A. Sun, J. Zhang, Reconstruction of pH-universal atomic Fe-N-C catalysts

[41] X. Wang, Z. Zhang, H. Gai, Z. Chen, Z. Sun, M. Huang, An efficient pH-universal electrocatalyst for oxygen reduction: defect-rich graphitized carbon shell wrapped cobalt within hierarchical porous N-doped carbon aerogel, Mater. Today Energy 17 (2020), 100452.

[42] Y. Xu, H. Zhang, P. Zhang, M. Lu, X. Xie, L. Huang, In situ exsolved Co components on wood ear-derived porous carbon for catalysing oxygen reduction over a wide pH range, J. Mater. Chem. A 9 (2021) 10695–10703.

[43] B. Zhou, F. Yan, X. Li, J. Zhou, W. Zhang, An interpenetrating porous organic polymer as a precursor for FeP/Fe_2P-embedded porous carbon toward a pH-universal ORR catalyst, ChemSusChem 12 (2019) 915–923.

[44] X. Ma, Z. Lei, W. Feng, Y. Ye, C. Feng, Living Fe mineral@bacteria encrustation-derived and self-templated preparation of a mesoporous Fe-N-C electrocatalyst with high activity for oxygen reduction, Carbon 123 (2017) 481–491.

[45] Z. Zhao, C. Chen, Z. Liu, J. Huang, M. Wu, H. Liu, Y. Li, Y. Huang, Pt-based nanocrystal for electrocatalytic oxygen reduction, Adv. Mater. 31 (2019) 1808115.

[46] S.K. Singh, K. Takeyasu, J. Nakamura, Active sites and mechanism of oxygen reduction reaction electrocatalysis on nitrogen-doped carbon materials, Adv. Mater. 31 (2019) 1804297.

[47] M. Liu, L. Wang, K. Zhao, S. Shi, Q. Shao, L. Zhang, X. Sun, Y. Zhao, J. Zhang, Atomically dispersed metal catalysts for the oxygen reduction reaction: synthesis, characterization, reaction mechanisms and electrochemical energy applications, Energy Environ. Sci. 12 (2019) 2890–2923.

[48] M.T.M. Koper, Analysis of electrocatalytic reaction schemes: distinction between rate-determining and potential-determining steps, J. Solid State Electrochem. 17 (2013) 339–344.

[49] A. Kulkarni, S. Siahrostami, A. Patel, J.K. Nørskov, Understanding catalytic activity trends in the oxygen reduction reaction, Chem. Rev. 118 (2018) 2302–2312.

[50] X. Zhang, X. Wang, L. Jiang, H. Wu, C. Wu, J. Su, Effect of aqueous electrolytes on the electrochemical behaviors of supercapacitors based on hierarchically porous carbons, J. Power Sources 216 (2012) 290–296.

towards oxygen reduction reaction, J. Colloid Interface Sci. 582 (2021) 1033–1040.